Estimating Site Response with Recordings from Deep Boreholes and HVSR: Examples from the Mississippi Embayment of the Central United States

Article *in* Bulletin of the Seismological Society of America · March 2018

DOI: 10.1785/0120170156

N. Seth Carpenter
University of Kentucky

Zhenming Wang
University of Kentucky

Edward Woolery
University of Kentucky

Bulletin of the Seismological Society of America, Vol. 108, No. 3A, pp. 1199–1209, June 2018, doi: 10.1785/0120170156

Estimating Site Response with Recordings from Deep Boreholes and HVSR: Examples from the Mississippi Embayment of the Central United States

by N. Seth Carpenter,* Zhenming Wang, Edward W. Woolery, and Mianshui Rong

Abstract Recordings of weak-motion *S* waves at two deep vertical seismic arrays in the northern Mississippi embayment (i.e., vertical seismic array Paducah [VSAP] and the Central United States Seismic Observatory [CUSSO]) were used to estimate empirical site responses using ratios of surface-to-bedrock transverse-component amplitude spectra TF_T. The mean TF_T curves were also compared with theoretical transfer functions derived from Thomson–Haskell propagator matrices. The results were comparable, indicating that mean spectral ratios, calculated from few (10) events at local and regional distances, represent empirical linear *S*-wave transfer functions for weak-motion *SH* waves at these sites. At both sites, the largest amplifications implied by the theoretical responses and the observed *S*-wave spectral ratios occur at frequencies higher than the sites' fundamental frequencies.

These spectral ratios were used to evaluate the suitability of surface *S*-wave horizontal-to-vertical spectral ratios HV_S for estimating the empirical site transfer function. The mean *S*-wave HV_S curves are similar to the mean TF_T spectral ratios for frequencies below approximately the fifth natural frequency at each site; for higher frequencies, vertical-component amplification from incident *SV* waves reduces HV_S relative to TF_T. Therefore, HV_S curves at these sites reflect the *SH*-wave transfer functions for low frequencies. We also observed that HV_S curves from ambient noise recordings do not estimate the *SH*-wave transfer function at these deep borehole sites for frequencies higher than the fundamental.

Introduction

Strong ground motion can be altered by near-surface soft sediments in terms of its duration, frequency content, and amplitude. This is called the site effect, and it can cause additional damage to susceptible buildings and infrastructure during earthquakes. A classic example of such damage is Mexico City, which was significantly damaged by amplified ground motions of near-surface lake sediments during the 1985 M_w 8.0 Michoacán earthquake (Seed *et al.*, 1988). Another example is the Marina District of San Francisco, which incurred significant damage from amplified ground motion in the San Francisco Bay muds during the 1989 M_w 6.9 Loma Prieta earthquake (Bonilla, 1991). Site effects are common phenomena during strong earthquakes, and continue to be a significant subject for seismological research (see, e.g., Fleur *et al.*, 2016; Woolery *et al.*, 2016).

Site effect is influenced by many factors, including lateral and vertical velocity gradients in the sediment and bedrock, impedance contrasts within the sediment overburden and at the sediment–bedrock interface, sediment thickness, sediment–bedrock interface geometry, incoming ground-motion amplitude (i.e., linear vs. nonlinear behavior), and surface topography. There are several established methods in practice for characterizing site effect, ranging between empirical and theoretical, but there are considerable attendant uncertainties (Steidl *et al.*, 1996), particularly in regions with deep sediment deposits (> 100 m), such as in the northern Mississippi embayment of the central United States. A direct way to study site effects, of particular importance for sites overlying thick sediment layers, is to simultaneously record earthquakes with a vertical array of downhole (i.e., bedrock) and surface sensors (Archuleta *et al.*, 1992; Margheriti *et al.*, 2000). The recordings from the two deep vertical seismic arrays in the northern Mississippi embayment, vertical seismic array Paducah (VSAP) and Central United States Seismic Observatory (CUSSO), permit direct evaluation of the site response in this deep-sediment setting.

*Also at Department of Earth and Environmental Sciences, University of Kentucky, 101 Slone Research Building, Lexington, Kentucky 40506-0053.

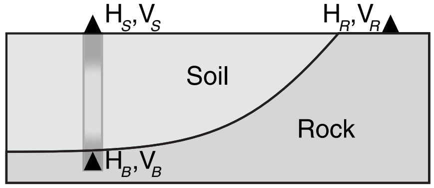

Figure 1. Locations of sensors (triangles) at the surface at soil (S) and rock-outcrop (R) sites, and beneath the soil in bedrock (B). H and V represent amplitude spectra of horizontal- and vertical-component recordings, respectively, at these locations.

In this study, we performed spectral analysis on the weak-motion *S*-wave recordings from VSAP and CUSSO to calculate the empirical transfer functions. We compared the mean empirical transfer functions with theoretical transfer functions derived from the Thomson–Haskell plane-wave reflectivity model for *SH* waves, focusing on frequencies of engineering interest. Then, we assessed whether mean transverse-to-vertical spectral ratios approximate the empirical transfer functions at these borehole sites.

This study represents an unprecedented effort to characterize site response directly using surface-to-bedrock spectral ratios in the thick northern Mississippi embayment sediment that overlies the active New Madrid seismic zone and underlies several large population centers, including Memphis, Tennessee. In addition, we use these spectral ratios to evaluate the use of horizontal-to-vertical spectral ratios (HVSRs; e.g., McNamara *et al.*, 2015; Hassani and Atkinson, 2016) to characterize site response in central and eastern North American.

Empirical *SH*-Wave Transfer Function and HVSR

The Fourier spectrum of ground acceleration for *SH* waves at a given site can be modeled as the convolution of source $S(f)$, path $P(f)$, site response $G(f)$, and instrument response $I(f)$ terms as

$$A(f) = S(f) \times P(f) \times G(f) \times I(f). \quad (1)$$

In the following, we use the quantities in equation (1) to derive expressions for the empirical site transfer function G from the *SH*-wave amplitude spectra A of recorded ground motions. We add subscripts of S, R, and B to equation (1) for horizontal (H) and vertical (V) amplitude spectra recorded at soil, rock outcrop, and borehole bedrock sites, respectively, as shown in Figure 1.

Empirical Transfer Function: Surface-to-Bedrock Spectral Ratios

If soil and rock-outcrop sites are proximal (i.e., differences in the source and path terms are negligible for both soil and rock sites: $S_S(f) \cong S_R(f)$ and $P_S(f) \cong P_R(f)$) and if the site response at the rock site G_R is assumed to be flat and to equal unity, then after removal of the instrument responses, the spectral ratio between soil and rock sites is

$$G_S = \frac{A_S}{A_R}. \quad (2)$$

When horizontal, transverse motions of S waves are considered, equation (2) is the transfer function for *SH* waves between the soil and rock sites that is traditionally used as the empirical site response in earthquake engineering (Borcherdt, 1970).

Depending on the source mechanism and the relative positions of the soil and rock sites to the source, however, the requirements of equation (2), that differences in the source and path terms for rock and soil sites are negligible, might not be applicable. An additional concern is that the rock site has its own site response (see, e.g., Steidl *et al.*, 1996) that is not accounted for in the above formulation. Another approach, which may abate these concerns, directly compares the acceleration spectra at the surface with those at the bedrock in a borehole (Fig. 1) (see, e.g., Joyner *et al.*, 1976; Steidl *et al.*, 1996). The ratio of the surface transverse-component amplitude spectrum to that in the bedrock for this configuration is

$$\mathrm{TF}_T = \frac{\mathrm{H}_S}{\mathrm{H}_B}, \quad (3)$$

which is the empirical *SH*-wave transfer function for a given angle of incidence from the bedrock.

Assuming that a plane-wave model for *SH* waves in an elastic 1D-layered structure is appropriate for the seismic waves recorded by VSAP and CUSSO, equation (3) can be expressed analytically using Thomson–Haskell matrices (Haskell, 1953, 1960), hereafter TH_{SH}.

Horizontal-to-Vertical Spectral Ratio

The HVSR was originally used to estimate site response using recordings of microtremors (Nakamura, 1989) and later from earthquake recordings (Lermo and Chavez-Garcia, 1993). HVSR is defined as the ratio of the horizontal H_S to the vertical amplitude spectra of ground motion V_S at the free surface:

$$\mathrm{HV}_S = \frac{\mathrm{H}_S}{\mathrm{V}_S}. \quad (4)$$

As previously stated, H_S represents the amplitude spectra of the transverse component of motion.

Equation (4) can be expanded as

$$\mathrm{HV}_S = \frac{\mathrm{H}_S}{\mathrm{H}_B} \times \frac{\mathrm{H}_B}{\mathrm{V}_B} \times \frac{\mathrm{V}_B}{\mathrm{V}_S}, \quad (5)$$

and equation (5) can be rewritten as

$$\mathrm{HV}_S = \mathrm{TF}_T \times \mathrm{HV}_B \times \frac{1}{\mathrm{TF}_V}, \quad (6)$$

in which HV_B is the HVSR in the bedrock and TF_V is the transfer function of vertical ground motions for a particular ray parameter. Horizontally polarized *SH* waves do not excite

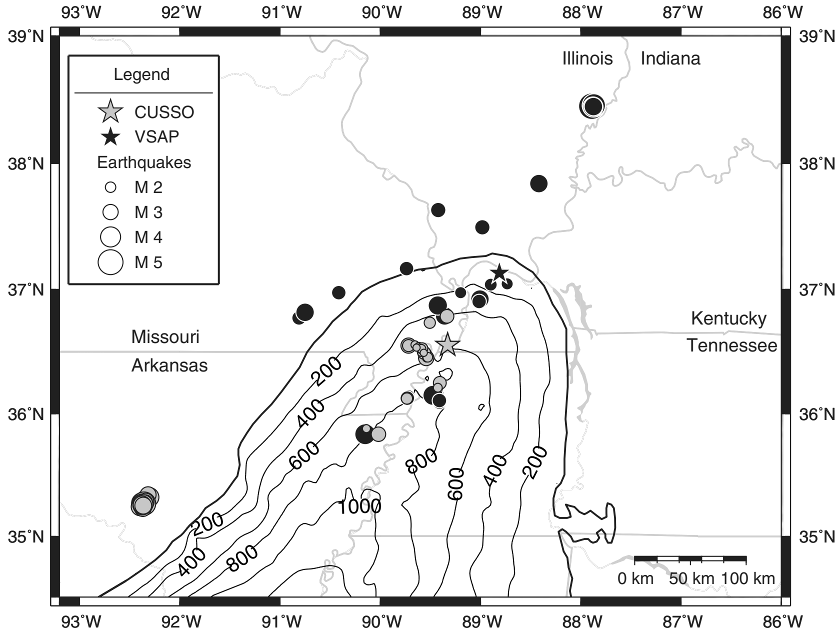

Figure 2. Vertical seismic arrays Central United States Seismic Observatory (CUSSO) (gray star) and vertical seismic array Paducah (VSAP) (black star) in the northern Mississippi embayment and the earthquakes they recorded (gray or black depending on the recording array). Embayment depth-to-bedrock contours are labeled by depth below the surface in meters. Contours (in meters) are sediment thickness from Dart (1992) and Dart and Swolfs (1998), modified from Langston *et al.* (2009).

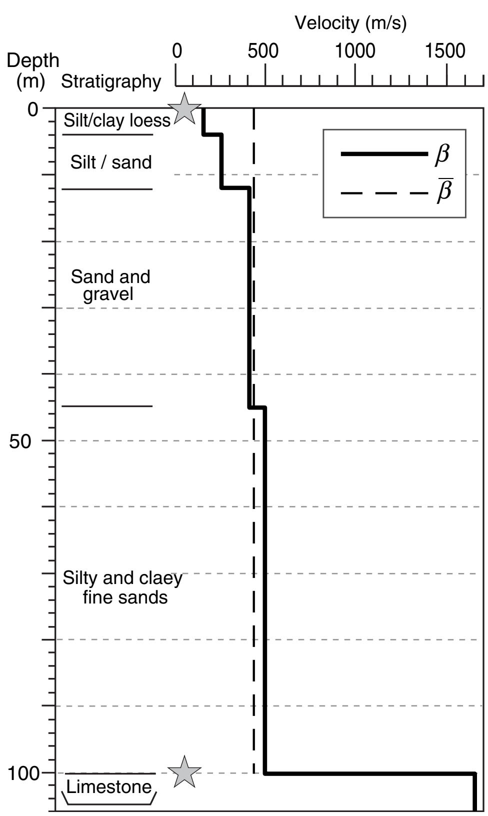

Figure 3. Simplified stratigraphic column, sensor depths (stars), and shear-wave velocity structure at VSAP. The average velocity shown (dashed line) was calculated for the entire sediment column, weighted by layer thickness.

vertical motions. Therefore, the vertical-component time series contains *SV* and *P* arrivals within the *S*-wave window, rather than *SH* waves.

Equation (6) shows that the surface HVSR HV_S is equal to the *SH*-wave transfer function in equation (3), expressed theoretically by TH_{SH} times the borehole HVSR HV_B divided by the vertical motion transfer function TF_V. Nakamura (1989) observed that HV_B is, on average, approximately unity for ambient noise. HV_B determined from recordings windowed around *S* waves, however, depends on the earthquake focal mechanism; therefore, because TF_T and TF_V are independent of the source, HV_S will also depend on the source mechanism. Our approach was to calculate the mean HV_S from multiple events to determine if, on average, HV_S approximates TF_T.

The denominator of equation (6) TF_V can be expressed analytically using Thomson–Haskell matrices for the *P*–*SV* system (Haskell, 1953, 1962). For recordings windowed around the *S* wave, the incident phases in the bedrock are assumed to be predominantly *SV* waves. Therefore, the transfer function in equation (17) from Haskell (1962) for an elastic 1D-layered structure, hereafter $TH_{SV,V}$, is used as the expression for TF_V in this investigation.

Vertical Arrays and Datasets

The settings of the vertical arrays used in this study differ in terms of unlithified sediment thicknesses, proximities to the edge of the embayment (Fig. 2), and age of the near-surface deposits. The geology, instrumentation, and recordings from VSAP and CUSSO are described briefly below.

VSAP

VSAP was installed near Paducah, Kentucky, in the early 1990s (Street *et al.*, 1997). The site is ~15 km from the edge of the northern Mississippi embayment on a 100-m-thick sequence of unlithified to poorly lithified silts, sands, clays, and gravels of Late Cretaceous to Pleistocene age overlying Mississippian limestone bedrock (Harris, 1992). Four soil layers and the bedrock were identified by two orthogonal *SH*-wave refraction profiles and incorporated into the velocity model of VSAP (McIntyre, 2008; Table 1; Fig. 3). The fundamental frequency f_0 of *S*-wave resonance in the overburden at this site for vertical incidence *S* waves (Haskell, 1960) is 1.06 Hz using

$$f_{n-1} = \frac{V_S}{4h}(2n-1), \qquad n = 1, 2, 3, \ldots, \tag{7}$$

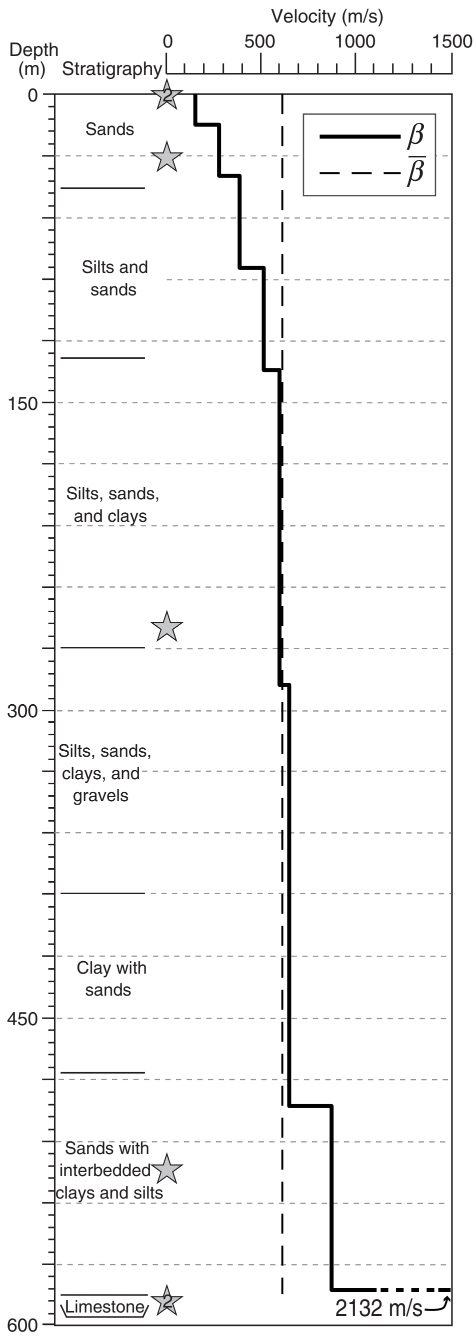

Figure 4. Simplified stratigraphic column, sensor depths (stars; locations with two sensors are labeled with a "2"), and shear-wave velocity structure at CUSSO. The average velocity shown (dashed line) was calculated for the entire sediment column, weighted by layer thickness.

in which V_S is the weighted-average S-wave velocity (i.e., layer velocities weighted by layer thickness), h is the thickness of the sediment overburden, and n is the resonance mode.

VSAP's recordings analyzed for this study were acquired from 1 May 2005 through April 2008. During this time, a $1/4g$ strong-motion accelerometer was installed in the bedrock and, at various times, either a $1g$ or a $2g$ strong-motion accelerometer operated at the free surface. The $1/4g$ and $2g$ sensors have flat responses to ground acceleration from d.c. to nominally 50 Hz; the $1g$ sensor's flat response extends from d.c. to a nominal 200 Hz. Data from the borehole and surface sensors were acquired at 200 samples per second.

Table 1
Soil-Profile Parameters for Site-Response Modeling at VSAP and CUSSO

Site	Thickness (m)	α (m/s)	β (m/s)
VSAP	4		150
	8		248
	33		400
	55		485
			1630
CUSSO	15	1000	160
	25	1550	280
	45	1600	390
	50	1650	515
	155	1850	600
	205	1900	650
	90	2300	875
		3669	2132

α, P-wave velocity, when available; β, S-wave velocity; CUSSO, Central United States Seismic Observatory; VSAP, vertical seismic array Paducah.

CUSSO

Phased installation of the three-borehole 21-component strong-motion array CUSSO began in 2005 and was completed in 2008. The deepest borehole penetrates the entire soil-sediment overburden (585 m) and is terminated 9 m into Ordovician limestone bedrock. The stratigraphy, the velocity model (Fig. 4; Table 1), and CUSSO's instrumentation and recordings are described in Woolery *et al.* (2016). For this study, we used recordings from the two medium-period seismometers (0.067–50 Hz flat-response passbands), installed at the surface and at 587-m depth, each acquired at 200 samples per second. From the S-wave velocity structure at CUSSO, f_0 is 0.23 Hz.

The bedrock S-wave velocity at CUSSO increases rapidly with depth from 1452 to 1810 m/s in 1 m (McIntyre, 2008), and it is uncertain if the velocity at the depth of the borehole sensor falls within this range. Also, it is unknown if the steep velocity gradient continues below this deepest measurement to produce the site's high-impedance boundary. Because of these unknowns, and our observations of large SH-wave amplifications, we adopted the maximum bedrock S-wave velocity observed at the nearby New Madrid test well 1-X (NMTW-1-X), 26 km southwest of CUSSO, as CUSSO's bedrock velocity. The depth to bedrock at the NMTW-1-X site is 616 m and, similar to CUSSO, Sexton and Jones (1986) reported S-wave velocities that increase rapidly with depth in the bedrock: 1200 m/s was observed at the top of bedrock, and the maximum of 2132 m/s occurred 4 m deeper.

Although the actual bedrock S-wave velocity at CUSSO is uncertain, the observed bedrock velocity at the

Table 2
Parameters for the Earthquakes Recorded by VSAP Used in This Study

Date (yyyy/mm/dd)	Time (hh:mm)	Latitude (°)	Longitude (°)	Depth (km)	Mag*	Dist (km)	BAZ (°)	iB (°)	iS (°)
2005/05/01	12:37	35.83	−90.15	10	4.2w	187	220	26	1
2005/06/02	11:35	36.15	−89.47	15	4.0w	124	209	24	1
2005/06/20	02:00	36.94	−88.99	7.7	2.7d	27	216	26	1
2005/06/20	12:21	36.92	−89	18.7	3.6w	28	216	21	1
2005/06/27	15:46	37.63	−89.42	9.6	3.0l	77	316	26	1
2006/01/02	21:48	37.84	−88.42	7.3	3.6l	86	204	26	1
2008/04/18	09:36	38.45	−87.89	14.2	5.2w	168	29	24	1
2008/04/18	15:14	38.46	−87.87	15.5	4.7w	169	29	24	1
2008/04/21	05:38	38.45	−87.88	18.3	4.0w	168	29	24	1
2010/03/02	19:37	36.79	−89.36	8.2	3.7l	61	232	24	1

Mag, event magnitude and type; Dist, epicenter VSAP offset; BAZ, VSAP epicenter back azimuth; iB, *S*-wave incidence angle at the bedrock sensor; iS, *S*-wave incidence angle at the surface.
*Magnitude types: w, moment magnitude; d, duration magnitude; l, m_{bLg}.

Table 3
Parameters for the Earthquakes Recorded by CUSSO Used in This Study

Date (yyyy/mm/dd)	Time (hh:mm)	Latitude (°)	Longitude (°)	Mag*	Depth (km)	Dist (km)	BAZ (°)	iB (°)	iS (°)
2010/05/30	02:24	36.55	−89.72	3.1d	9.2	34	269	19	1
2010/06/09	18:40	36.25	−89.4	2.5d	5.2	34	191	19	1
2011/02/17	10:49	35.28	−92.36	3.8w	6.5	308	243	15	1
2011/02/18	04:59	35.26	−92.37	3.9w	5	310	243	14	1
2011/02/18	8:13	35.27	−92.38	4.1w	6.2	310	244	15	1
2011/02/28	05:00	35.27	−92.35	4.7w	3.1	308	243	15	1
2011/03/03	15:31	35.27	−92.37	3.0d	6	309	243	15	1
2011/03/04	08:45	35.28	−92.34	2.8d	3	306	243	15	1
2011/04/08	03:27	35.26	−92.39	3.2l	5.5	311	243	15	1
2011/04/08	14:56	35.26	−92.36	3.9w	6.2	309	243	14	1

Mag, event magnitude and type; Dist, epicenter-CUSSO offset; BAZ, CUSSO epicenter back azimuth; iB, *S*-wave incidence angle at the bedrock sensor; iS, *S*-wave incidence angle at the surface.
*Magnitude types: w, moment magnitude; d, duration magnitude; l, m_{bLg}.

NMTW-1-X well produces theoretical amplifications that are much more consistent with our observations (see the Results and Discussion sections) than those from a slower velocity. We therefore use this velocity as the bedrock velocity in our site velocity model. However, the theoretical *SH*-wave transfer function calculated for CUSSO is provisional until this velocity is validated with an independent method.

Methods

Data Selection and Processing

Both CUSSO and VSAP recorded few events each (Fig. 2), due to their brief operational time spans. In addition, no strong ground motions (i.e., greater than 50 cm/s^2) were recorded by these stations. Therefore, selecting high-quality recordings of the weak motions is imperative to avoid contaminating the spectral ratios and their averages with noise. Our quality assessments included inspection of waveforms, the corresponding amplitude spectra, and signal-to-noise calculations in the frequency domain. Records that contained instrument glitches or spikes in the *S*-wave window were excluded from the analyses, and only recordings with pre-*P*-wave noise and signal-to-noise ratios exceeding 1.5 for each component and for frequencies from the site f_0 to 25 Hz were analyzed. Parameters of the local and regional earthquakes used for this study are listed in Tables 2 and 3.

We converted each triggered waveform file to Seismic Analysis Code format, removed the mean and trend, and then deconvolved the instruments responses to yield ground acceleration time histories (seismometer recordings at CUSSO were converted from ground velocity to acceleration), using the processing parameters shown in Table 4. We rotated the

Table 4
Data Processing Parameters for Recordings at VSAP and CUSSO

Station	t_0 (s)	t_{win} (s)	Taper (%)	f_{lo}/f_{hi} (Hz)	f_{smooth} (Hz)
VSAP	0.25	5.0	5	0.07/40	0.5
CUSSO	1.0	20.0	5	0.07/40	0.1

t_0, window start time prior to *SH*-wave arrival; t_{win}, window length around *SH* wave; Taper, percentage of window length tapered with Hanning window; f_{lo}/f_{hi}, low and high corner frequencies for two-pole zero-phase Butterworth band-pass filter; f_{smooth}, length of running-average smoothing filter used to smooth amplitude spectra.

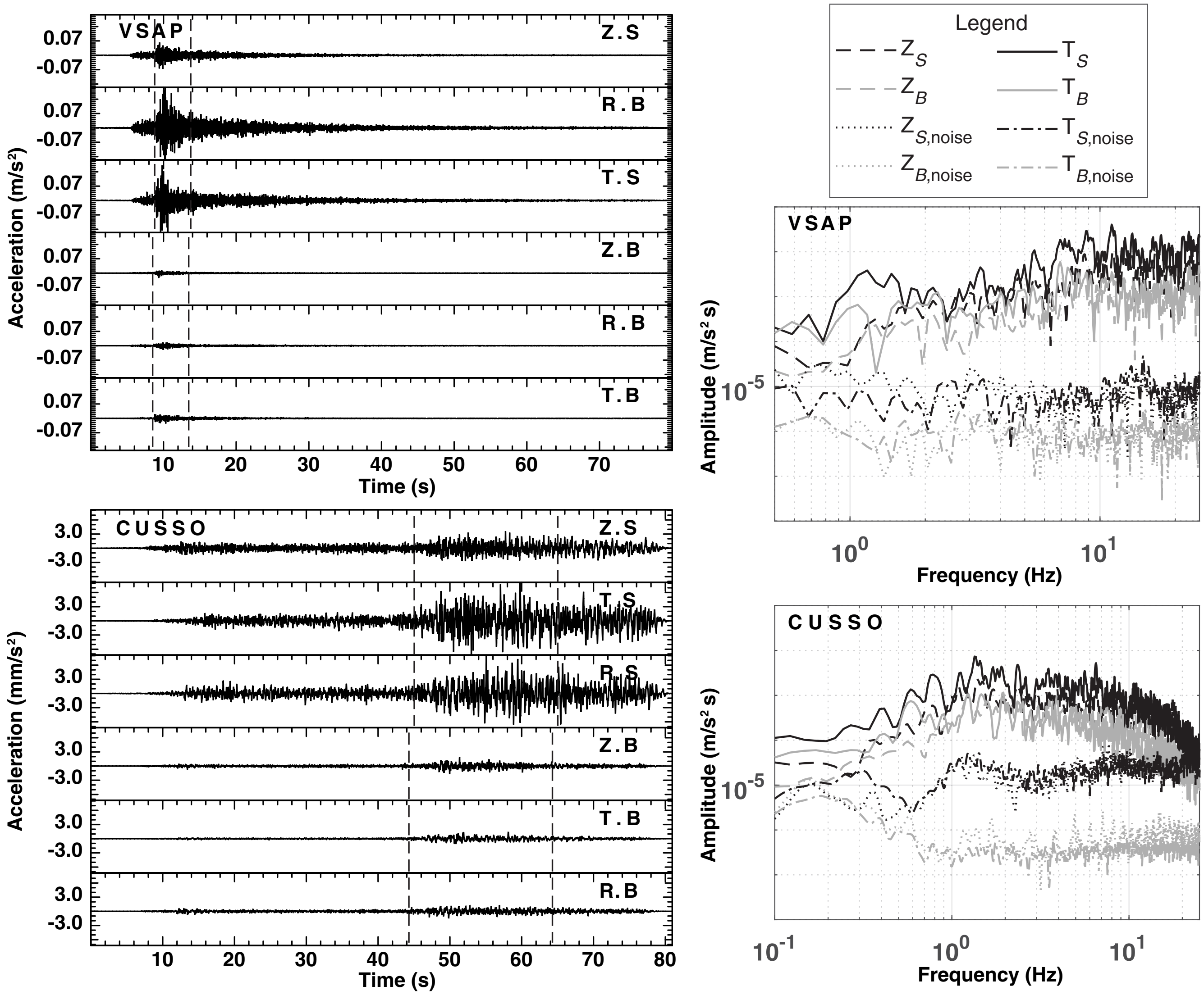

Figure 5. (Left) Time histories and (right) amplitude spectra from the 2 January 2006 M_w 3.6 local earthquake recorded at (top row) VSAP and the 28 February 2011 M_w 4.7 regional earthquake recorded at (bottom row) CUSSO. Surface traces (upper three traces in each row) and bedrock traces (lower three traces in each row) are shown and labeled by channel name. Amplitude spectra are calculated from the windowed portion (dashed lines) of each waveform; noise spectra were determined from the waveforms prior to the first *P*-wave arrival (entire time windows not shown).

surface and borehole horizontal-component recordings to radial and transverse orientations. Figure 5 shows example accelerograms and their corresponding amplitude spectra.

Because both sites are over thick layers of unconsolidated sediment, we used relatively long *S*-wave windows of five times the sites' fundamental periods (i.e., f_0^{-1}) to resolve the amplification at each site's fundamental frequency. Shorter windows do not provide adequate resolution at low frequencies, due to the weak motions recorded by these arrays. For local events (offset < ~100 km), windowed, transverse-component recordings will principally contain direct *SH* waves, with some scattered *SH*-wave and *Lg*-wave phases. At larger offsets, the transverse-component *S*-wave windows, which avoid *Rg* waves, can contain arrivals from *Sn*, direct *SH*, and *Lg* waves. Although this diversity of phases are potentially included in spectral ratios from individual events, we found that most peaks in the mean TF_T curves from local events and from regional events occur at the frequencies predicted by TH_{SH}, calculated for average incidence angles (Tables 2 and 3). This consistency indicates that the arrivals included in the *S*-wave windows produce resonances in the soil columns consistent with direct *SH*-wave resonance. For vertical-component recordings, energy in the *S*-wave windows comes primarily from incident *SV* waves that are transmitted as *P* and *SV* waves, as demonstrated for CUSSO in the Discussion section.

Figure 6 summarizes the dataset in terms of the spatial distribution of the events with respect to the stations. The largest surface ground motion at VSAP, 23.0 cm/s², was produced by a moment magnitude (M_w) 3.6 earthquake

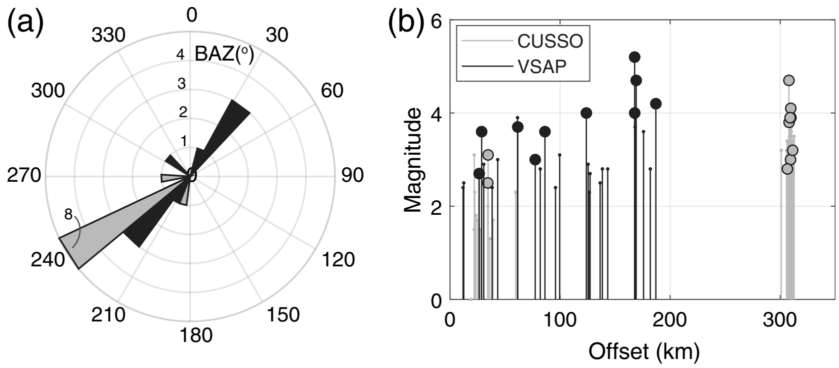

Figure 6. (a) Polar-plot histogram of back azimuths (azimuth from station to event) for events listed in Tables 2 and 3 for VSAP (black) and CUSSO (gray). (b) Magnitude versus offset for all events recorded by VSAP and CUSSO. Lines corresponding to events listed in Tables 2 and 3 are tipped with large circles.

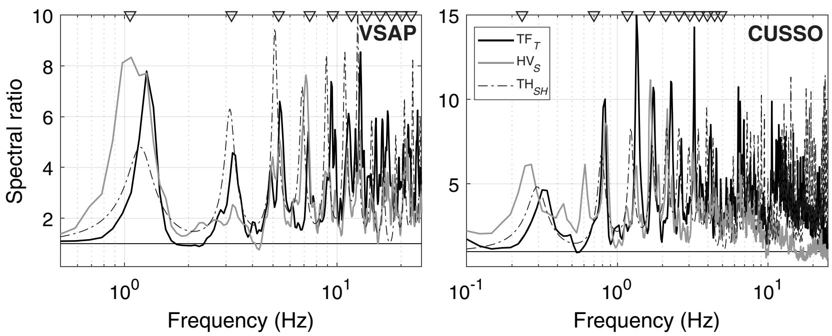

Figure 7. Mean spectral ratios from recordings at VSAP and CUSSO and theoretical Thomson–Haskell *SH*-wave transfer functions (TH_{SH}) for average bedrock incidence angles of 25° at VSAP and 15° at CUSSO. Inverted triangles correspond to the fundamental and 10 next higher natural frequencies from equation (7). Solid horizontal line indicates a ratio of 1 in each plot.

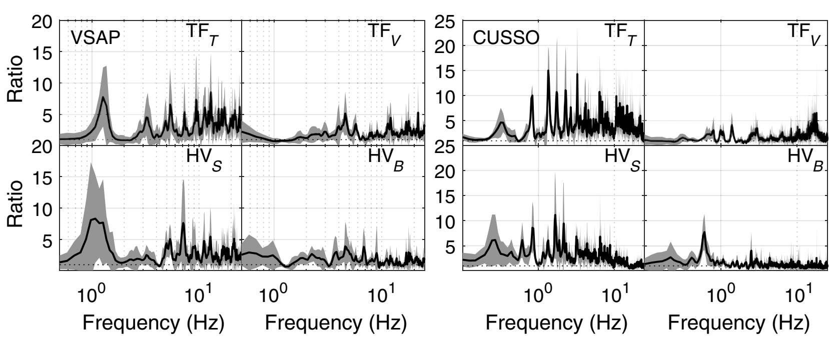

Figure 8. Mean spectral ratios shown in Figure 7 (heavy black) and mean ±1 standard deviation regions (solid gray). Dotted horizontal line indicates a ratio of 1 in each plot.

29 km southwest of VSAP (Fig. 5). Three of the earthquakes recorded at VSAP were associated with the 2008 M_w 5.2 Mount Carmel, Illinois, earthquake sequence (Hamburger *et al.*, 2011), including the mainshock. All but two of the earthquakes recorded at CUSSO listed in Table 3 occurred in Arkansas and were associated with the Guy-Greenbrier sequence between 2010 and 2011 (Horton, 2012). The largest ground motion recorded at the surface at CUSSO was 1.0 cm/s^2, from the duration magnitude (M_D) 3.1 local earthquake on 30 May 2010.

We also calculated HVSRs from continuous recordings of ambient noise at the free surface $HV_{S,\text{noise}}$ to evaluate its ability to resolve the *SH*-wave transfer function as per the Nakamura (1989) approach. Satoh *et al.* (2001), among others, reported differences between HV_S and $HV_{S,\text{noise}}$ in terms of the frequency of maximum amplification, f_{peak}, and amplification levels. We used 5 hrs of nighttime ambient noise (to reduce cultural noise), uncontaminated by earthquakes or blasts, recorded by CUSSO's existing surface seismometer and from a temporary broadband seismometer collocated with VSAP's surface accelerometer.

Spectral Ratios

Using the bedrock and surface amplitude spectra for the events listed in Tables 2 and 3, we calculated the mean spectral ratios TF_T, TF_V, HV_S, and HV_B and their standard deviations at VSAP and CUSSO. Individual spectral ratios were calculated by spectral division of the smoothed amplitude spectra. The amplitude spectra of all recordings at the free surface were divided by a factor of 2 to remove the effect of free-surface amplification for equivalency with traditional spectral ratios (equation 2) and for comparison with HV_S. This division by 2 may not strictly be valid for TF_V and is discussed in the Discussion section.

The mean $HV_{S,\text{noise}}$ spectral ratios were determined by first averaging the spectral ratios of smoothed (moving window lengths in Table 4) amplitude spectra calculated from the 5-min-long 50% overlapping windows of 5 hrs of continuous recordings. Because the sources of ambient noise are likely from a suite of azimuths, recorded on both horizontal components, we calculated $HV_{S,\text{noise}}$ curves from the average spectrum of both horizontal components divided by the average vertical-component spectrum of both horizontal components.

Results

Figures 7 and 8 show mean TF_T, TF_V, HV_S, and HV_B curves, the corresponding standard deviations for VSAP and

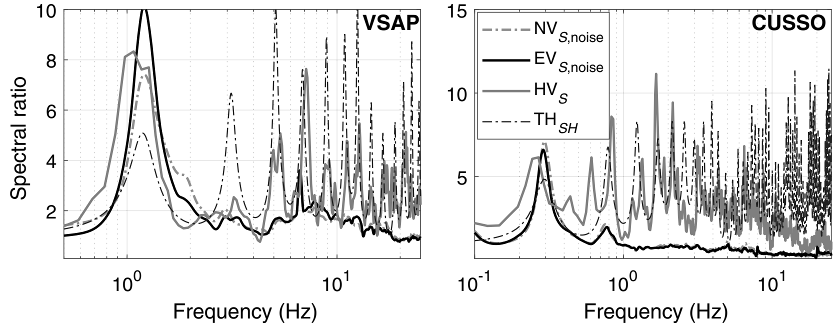

Figure 9. Horizontal-to-vertical spectral ratio (HVSR) curves derived from 5 hrs of ambient noise, $NV_{S,\mathrm{noise}}$ and $EV_{S,\mathrm{noise}}$, for the north and east components, respectively, recorded at VSAP and CUSSO. For comparison, S-wave HVSR HV_S and the theoretical Thomson–Haskell SH-wave transfer function TH_{SH} are also shown.

CUSSO, and the predicted *SH*-wave responses from Thomson–Haskell propagator matrices TH_{SH} (divided by 2 for consistency with TF_T and HV_S). In general, there is remarkable consistency between TF_T and HV_S, particularly within the frequency band of engineering interest (0.1–10 Hz), in terms of the peak frequencies. At the first peak frequency (hereafter referred to as observed-f_0), amplifications implied by both TF_T and HV_S are very similar. Furthermore, Figure 7 shows that peak frequencies of both TF_T and HV_S correspond closely with the fundamental and higher-mode resonances predicted by equation (7) for vertical-incidence *S* waves and to TH_{SH}, calculated at average incidence angles.

The mean ± one standard deviations (Fig. 8) demonstrate that the spectral ratios' peak frequencies are generally consistent between events, regardless of distance (which was also observed by Zandieh and Pezeshk, 2011) for HV_S. However, HV_S has greater variability and resolves observed-f_0 with less resolution than TF_T, based on HV_S having broader half-widths of the lowest frequency peaks. It is possible that some of the variability in the peak frequencies is due to nonlinear responses. Rubinstein (2011) reported evidence of nonlinear response for ground accelerations as low as $34\ \mathrm{cm/s^2}$, which is comparable with the largest acceleration observed at VSAP of $24\ \mathrm{cm/s^2}$. We examined the spectral ratios from individual events and found that observed-f_0 does not decrease with PGA, which we interpret as evidence that no nonlinearity was experienced.

The HVSR curves calculated from recordings of ambient noise $HV_{S,\mathrm{noise}}$ at both sites are plotted in Figure 9. There are important differences between *S*-wave spectral ratios and $HV_{S,\mathrm{noise}}$ curves for frequencies greater than observed-f_0, as discussed in the next section.

Discussion

Empirical and Theoretical *SH*-Wave Transfer Functions

At both sites, TF_T, the empirical *SH*-wave transfer function is similar to the theoretical *SH*-wave transfer function from the elastic Thomson–Haskell propagator matrix method TH_{SH} for average and for vertical bedrock incidence angles. Evidently, the large impedance contrast between the northern Mississippi embayment sediment overburden and the bedrock bends transverse-wave arrivals from a range of bedrock incidence angles to nearly vertical incidence at the surface. Consequently, averaging the spectral ratios from transverse-component recordings of direct, head, and *Lg* waves reveals empirical *SH*-wave site responses suitable for engineering purposes. Furthermore, the similarities between TF_T and TH_{SH} indicate that 2D and 3D effects do not contribute significantly to the site responses at the VSAP and CUSSO sites. However, 1D site response models might not be applicable nearer to the edge of the embayment, due to basin-edge effects, as observed by Ramírez-Guzmán *et al.* (2012) and modeled by MacPherson *et al.* (2010), or in settings with complicated subsurface structures. In addition, the similarity between TF_T at VSAP and CUSSO and the corresponding theoretical responses, which do not include anelasticity, also supports the observations of relatively low intrinsic attenuation for body waves in the Mississippi embayment made by Langston (2003).

The TF_T curves show significant *SH*-wave amplification at peak frequencies from the fundamental to higher than the tenth natural frequency at each site. The maximum observed amplification factors from the TF_T curves are 8.5 ± 6.2 at 12.9 Hz (seventh natural frequency) at VSAP and 15.0 ± 4.8 at 1.3 Hz (third natural frequency) at CUSSO. The theoretical *SH*-wave transfer functions predict amplifications of 10.1 at VSAP and 8.3 at CUSSO for the peaks nearest to 12.9 and 1.3 Hz, respectively. At observed-f_0, amplification at VSAP is 7.8 ± 5.0 and 4.6 ± 2.5 at CUSSO. For comparison, an amplification of 4.8 is predicted by the theoretical *SH*-wave transfer functions at f_0 at both sites. The theoretical responses at CUSSO are provisional and require validation of the bedrock *S*-wave velocity that we used in this study. Nevertheless, the bedrock velocity employed is apparently reasonable, as evidenced by the similarities between the observed amplifications and the theoretical *SH*-wave response.

S-Wave HVSR

Peak amplifications implied by HV_S are similar to peak TF_T amplifications: the maxima are 8.3 ± 7.0 at VSAP at 1.1 Hz and 11.1 ± 8.7 at CUSSO at 1.7 Hz. The theoretical *SH*-wave transfer functions predict amplifications of 4.8 at VSAP and 7.2 at CUSSO for the peaks nearest to 1.1 and 1.7 Hz, respectively. At observed-f_0, amplifications are 8.3 ± 7.0 at VSAP and 6.1 ± 5.1 at CUSS0; 4.8 is the theoretical amplification at both sites at f_0.

Below a site-specific frequency, mean TF_T and HV_S curves are similar for both VSAP and CUSSO, and they resemble the theoretical *SH*-wave transfer functions at each

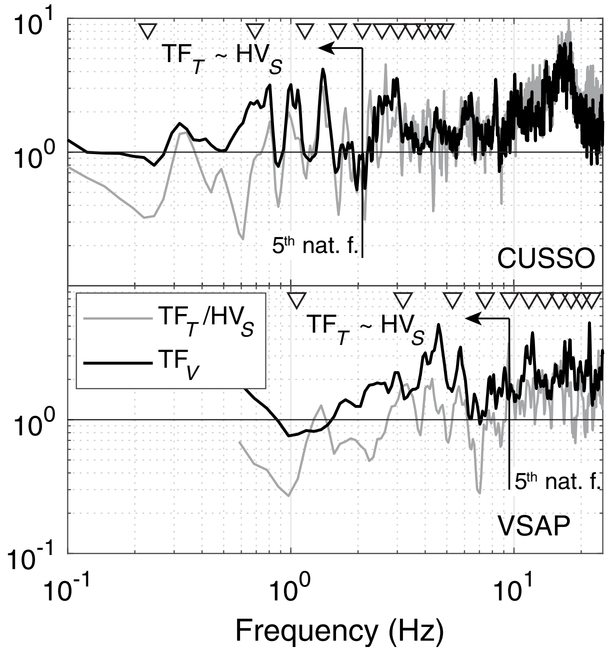

Figure 10. Vertical-component amplification TF_V and the ratio of spectral ratios TF_T to HV_S at CUSSO and VSAP. The fifth natural frequency (5th nat. f.), below which HV_S approximates TF_T, is labeled. Inverted triangles correspond to the resonance frequencies in equation (7).

site. However, there are differences between TF_T and HV_S that are made clear by their ratio (Fig. 10): for frequencies above approximately the fifth natural frequencies (~9 and ~2.0 Hz at VSAP and CUSSO, respectively), HV_S is consistently less than the observed *SH*-wave transfer function at both sites. This difference is much greater at the deeper-soil site CUSSO. At lower frequencies, the ratios of TF_T to HV_S tend to oscillate about one. At these frequencies, the differences are due, at least in large part, to slight differences in the peak frequencies rather than to differences in amplification; HV_S peaks occur at slightly lower frequencies than TF_T. For example, at both stations, Figure 10 suggests that HV_S yields greater amplification than TF_T by a factor of 2–3 for frequencies near f_0. However, the differences of the amplifications at the respective observed-f_0 are much less: 7% at VSAP and 25% at CUSSO.

The curves in Figure 10 also indicate that the differences between HV_S and TF_T are due to vertical-component amplification. The influence of TF_V on HV_S is shown in equation (6): HV_S is indirectly related to TF_V, and when HV_B is nearly one, as at CUSSO (Fig. 8), the ratio of TF_T to HV_S should be TF_V. At VSAP, HV_B is more complicated than at CUSSO and is generally greater than one. As such, the ratio of TF_T to HV_S is generally greater than TF_V. However, at both stations, the two curves in Figure 10 are correlated, demonstrating the strong control of the vertical-component transfer function on HV_S. Therefore, the ability of HV_S to approximate TF_T depends on TF_V.

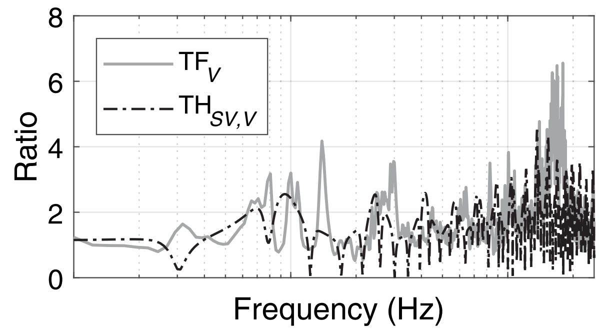

Figure 11. Observed TF_V and the predicted $TH_{SV,V}$ vertical-component amplification for an *SV* wave with an angle of incidence of 15° at CUSSO.

We found that TF_V is consistent with the vertical response predicted by Thomson–Haskell propagator matrices for incident *SV* waves, $TH_{SV,V}$ (Haskell, 1953, 1962), as shown in Figure 11. Therefore, the major differences between TF_T and HV_S (Fig. 10) are explained by the amplification of transmitted *SV* waves and converted *P* and *SV* waves. Furthermore, HV_S will more accurately approximate the *SH*-wave transfer function when corrected for TF_V (equation 6), which can be calculated by plane-wave propagation matrices. The similarity of the curves in Figure 11 also suggests that, for the steeply ascending waves recorded by both arrays, it appears to be reasonable to correct for free-surface amplification on the vertical component by division by a factor of 2, which was done to be consistent with TF_V. A thorough treatment of this particular topic is beyond the scope of this article.

Ambient Noise HVSR

Figure 9 compares $HV_{S,\text{noise}}$ curves with HV_S and the theoretical *SH*-wave responses and reveals that $HV_{S,\text{noise}}$ clearly identifies the fundamental site frequency, as observed in numerous studies (see, e.g., Nakamura, 1989; Bodin and Horton, 1999; Langston, *et al.*, 2009). At both stations, the amplification of the first peak of $HV_{S,\text{noise}}$ from either horizontal component is similar to HV_S. Therefore, $HV_{S,\text{noise}}$ is effective in both identifying the site f_0 and indicating the level of amplification at or near the site f_0. Higher-mode resonances, however, are not clearly identified with $HV_{S,\text{noise}}$, suggesting the presence of additional phase arrivals with energetic vertical motions. Therefore, although this methodology may be useful to calculate an average shear-wave velocity model, it does not reveal the frequencies at which peak amplifications occur (seventh and third natural frequencies at VSAP and CUSSO, respectively), nor their magnitudes, and is not suitable for studies of detailed velocity structure or site response.

On the Applicability of HVSR

Our observations suggest that the ability of *S*-wave and ambient-noise HVSRs to approximate the site transfer function in the northern Mississippi embayment at frequencies of engineering importance depends on the site's natural frequencies. Both HV_S and $HV_{S,\mathrm{noise}}$ approximate site response at f_0. However, if higher modes occur at frequencies of engineering interest, they will not be revealed by $HV_{S,\mathrm{noise}}$ and may be underestimated by HV_S, due to the amplification of high-frequency vertical motions. This is important because f_{peak} may not correspond with f_0 in the embayment, as at VSAP and CUSSO, and therefore maximum amplification may not be observable by HVSR. However, HV_S estimates the site response for frequencies up to the fifth natural frequency, which may be sufficient for sites over thinner ($< \sim 100$ m) sediment layers or that have faster sediment *S*-wave velocity structures.

In addition, Rong *et al.* (2016) demonstrated that HV_S curves estimate the nonlinear site transfer function in cases of strong ground motions. Therefore, HV_S may be useful for estimating the nonlinear site transfer function in the embayment, because HV_S reliably approximates the site response at lower frequencies and because high-frequency responses are decreased due to nonlinear effects (e.g., see Rong *et al.*, 2016). This will be evaluated when strong motions are recorded by VSAP and CUSSO.

Conclusions

Weak-motion *S*-wave recordings at the two deep vertical seismic arrays in the northern Mississippi embayment VSAP and CUSSO were used to estimate site responses using the spectral ratio method. The maximum observed amplification factors from the mean empirical *SH*-wave transfer functions are 8.5 ± 6.2 at 12.9 Hz at VSAP and 15.0 ± 4.8 at 1.3 Hz at CUSSO. We compared the spectral ratios with Thomson–Haskell propagator matrices and found that, although only 10 *S*-wave recordings at each array were suitable for analysis, the frequencies of the theoretical site response peaks were consistent with those from observed *SH*-wave surface-to-bedrock spectral ratios TF_T from local and regional earthquakes, thus indicating that TF_T represents an empirical *SH*-wave transfer function for weak motions. Theoretical and observed amplifications were also comparable, which indicates the appropriateness of 1D site-response modeling at these sites, but the theoretical levels of amplification at CUSSO are provisional because the bedrock *S*-wave velocity is uncertain.

TF_T curves were also used to evaluate the appropriateness of surface *S*-wave HVSR, HV_S, to estimate the empirical site transfer function. The observed HV_S curves are similar to the TF_T spectral ratios at frequencies below approximately the fifth natural frequency at each site, indicating that the HV_S curves can be used as single-station empirical approximations of the *S*-wave transfer functions for low-frequency analyses. For higher frequencies, vertical-component amplifications of incident *SV* waves and the converted *P*- and *SV*-wave systems reduce HV_S and cause it to deviate from observed *SH*-wave amplification at both VSAP and CUSSO. Therefore, the applicability of HV_S to approximate TF_T is site specific and depends on a site's vertical-component transfer function.

Finally, HVSR curves from ambient-noise recordings $HV_{S,\mathrm{noise}}$ imply amplification levels that are consistent with those indicated by the observed and theoretical *SH*-wave transfer functions. However, $HV_{S,\mathrm{noise}}$ curves at both sites decrease rapidly with frequency and do not contain important peaks in the *SH*-wave transfer functions at either site. Most importantly, $HV_{S,\mathrm{noise}}$ fails to reveal the frequencies at which the maximum amplifications occur in the frequency band of engineering interest (i.e., from 0.1 to 10 Hz) and the corresponding amplification levels; the largest amplifications observed by the *S*-wave spectral ratios occur at resonances higher than the sites' fundamental frequencies. Therefore, it appears that ambient noise HVSR cannot be used for detailed site-response analyses in the northern Mississippi embayment.

Data and Resources

Vertical seismic arrays VSAP and CUSSO are part of the Kentucky Seismic and Strong Motion Network (Kentucky Geological Survey/University of Kentucky [1982]: Kentucky Seismic and Strong Motion Network, University of Kentucky, Other/Seismic Network, doi: 10.7914/SN/KY), operated by the University of Kentucky. Recordings from these arrays are available for download from http://www.uky.edu/KGS/geologichazards/data.htm (last accessed May 2017). The hypocenters and magnitudes in Tables 2 and 3 are from the Center for Earthquake Research and Information catalog http://www.memphis.edu/ceri/seismic/catalog.php (last accessed February 2017). The map was made using Generic Mapping Tools (www.soest.hawaii.edu/gmt, last accessed February 2017).

Acknowledgments

The authors are grateful for the insights, comments, and reviews that they received from Martin Chapman, Chuck Langston, Tom Pratt, Bill Stephenson, and an anonymous reviewer, all of whom helped to greatly improve this article. The authors thank Meg Smath of the Kentucky Geological Survey for her editorial help. The authors acknowledge the insight and effort of Ron Street in installing the vertical seismic array in Paducah, Kentucky, and conceiving of the deep CUSSO vertical array. Funding for this study was provided by the Kentucky Geological Survey. The Kentucky Seismic and Strong-Motion Network is operated and maintained by the Kentucky Geological Survey and the Department of Earth and Environmental Sciences and the University of Kentucky.

References

Archuleta, R. J., S. H. Seale, P. V. Sangas, L. M. Baker, and S. T. Swain (1992). Garner valley downhole array of accelerometers: Instrumentation and preliminary data analysis, *Bull. Seismol. Soc. Am.* **82,** 1592–1621.

Bodin, P., and S. Horton (1999). Broadband microtremor observation of basin resonance in the Mississippi embayment, Central U.S., *Geophys. Res. Lett.* **26,** no. 7, 903–906.

Bonilla, M. G. (1991). The Marina District, San Francisco, California: Geology, history, and earthquake effects, *Bull. Seismol. Soc. Am.* **81,** 1958–1979.

Borcherdt, R. D. (1970). Effects of local geology on ground motion near San Francisco Bay, *Bull. Seismol. Soc. Am.* **60,** no. 1, 29–61.

Dart, R. L. (1992). Catalog of pre-Cretaceous geologic drill-hole data from the upper Mississippi embayment: A revision and update of open-file report 90-260, *U.S. Geol. Surv. Open-File Rept. 92-685*.

Dart, R. L., and H. S. Swolfs (1998). Contour mapping of relic structures in the Precambrian basement of the Reelfoot rift, North American midcontinent, *Tectonics* **17,** 235–249.

Fleur, S. S., E. Bertrand, F. Courboulex, B. M. Lépinay, A. Deschamps, S. Hough, G. Cultrera, D. Boisson, and C. Prépetit (2016). Site effects in Port-au-Prince (Haiti) from the analysis of spectral ratio and numerical simulations, *Bull. Seismol. Soc. Am.* **106,** doi: 10.1785/0120150238.

Hamburger, M. W., K. Shoemaker, S. Horton, H. DeShon, M. Withers, G. L. Pavlis, and E. Sherrill (2011). Aftershocks of the 2008 Mt. Carmel, Illinois, earthquake: Evidence for conjugate faulting near the termination of the Wabash Valley fault system, *Seismol. Res. Lett.* **82,** no. 5, 735–747.

Harris, J. (1992). Site amplification of seismic ground motions in the Paducah, Kentucky, area, *Ph.D. Thesis*, University of Kentucky, Lexington, Kentucky, 775 pp.

Haskell, N. A. (1953). The dispersion of surface waves on multilayered media, *Bull. Seismol. Soc. Am.* **43,** no. 1, 17–34.

Haskell, N. A. (1960). Crustal reflection of plane *SH* waves, *J. Geophys. Res.* **65,** no. 12, 4147–4150.

Haskell, N. A. (1962). Crustal reflection of plane *P* and *SV* waves, *J. Geophys. Res.* **67,** no. 12, 4751–4768.

Hassani, B., and G. M. Atkinson (2016). Applicability of the site fundamental frequency as a V_{S30} proxy for central and eastern North America, *Bull. Seismol. Soc. Am.* **106,** no. 2, 653–664.

Horton, S. (2012). Disposal of hydrofracking waste fluid by injection into subsurface aquifers triggers earthquake swarm in central Arkansas with potential for damaging earthquake, *Seismol. Res. Lett.* **83,** no. 2, 250–260.

Joyner, W. B., R. E. Warrick, and A. A. Oliver (1976). Analysis of seismograms from a downhole array in sediments near San Francisco Bay, *Bull. Seismol. Soc. Am.* **66,** no. 3, 937–958.

Langston, C. A. (2003). Local earthquake wave propagation through Mississippi embayment sediments, part I: Body-wave phases and local site responses, *Bull. Seismol. Soc. Am.* **93,** no. 6, 2664–2684.

Langston, C. A., S. C. C. Chiu, Z. Lawrence, P. Bodin, and S. Horton (2009). Array observations of microseismic noise and the nature of H/V in the Mississippi embayment, *Bull. Seismol. Soc. Am.* **99,** no. 5, 2893–2911.

Lermo, J., and F. Chavez-Garcia (1993). Site effect evaluation using spectral ratios with only one station, *Bull. Seismol. Soc. Am.* **83,** 1574–1594.

Macpherson, K. A., E. W. Woolery, Z. Wang, and P. Liu (2010). Three-dimensional long-period ground-motion simulations in the upper Mississippi embayment, *Seismol. Res. Lett.* **81,** no. 2, 391–405.

Margheriti, L., R. M. Azzara, M. Cocco, A. Delladio, and A. Nardi (2000). Analysis of borehole broadband recordings: Test site in the Po basin, northern Italy, *Bull. Seismol. Soc. Am.* **90,** no. 6, 1454–1463.

McIntyre, J. L. (2008). An evaluation of earthquake ground-motion site effects at two sites underlain by deep soils in western Kentucky, *Master's Theses*, University of Kentucky, Paper 562.

McNamara, D. E., W. J. Stephenson, J. K. Odum, R. A. Williams, and L. Gee (2015). Site response in the eastern United States: A comparison of V_{S30} measurements with estimates from horizontal:vertical spectral ratios, *Geol. Soc. Am. Spec. Pap.* **509,** pp. 67–79.

Nakamura, Y. (1989). A method for dynamic characteristics estimation of subsurface using microtremor on ground surface, *Q. Rep. Railway Tech. Res. Inst.* **30,** no. 1, 25–33.

Ramírez-Guzmán, L., O. S. Boyd, S. Hartzell, and R. A. Williams (2012). Seismic velocity model of the central United States (version 1): Description and simulation of the 18 April 2008 Mt. Carmel, Illinois, earthquake, *Bull. Seismol. Soc. Am.* **102,** no. 6, 2622–2645.

Rong, M., Z. Wang, E. W. Woolery, Y. Lyu, X. Li, and S. Li (2016). Nonlinear site response from the strong ground-motion recordings in western China, *Soil Dynam. Earthq. Eng.* **82,** 99–110.

Rubinstein, J. L. (2011). Nonlinear site response in medium magnitude earthquakes near Parkfield, California, *Bull. Seismol. Soc. Am.* **101,** no. 1, 275–286.

Satoh, T., H. Kawase, and S. Matsushima (2001). Differences between site characteristics obtained from microtremors, *S*-waves, *P*-waves, and codas, *Bull. Seismol. Soc. Am.* **91,** 313–334.

Seed, H. B., M. P. Romo, J. I. Sun, A. Jaime, and J. Lysmer (1988). The Mexico earthquake of September 19, 1985—Relationships between soil conditions and earthquake ground motions, *Earthq. Spectra* **4,** 687–729.

Sexton, J. L., and P. B. Jones (1986). Evidence for recurrent faulting in the New Madrid seismic zone from Mini-Sosie high-resolution reflection data, *Geophysics* **51,** no. 9, 1760–1788.

Steidl, J. H., A. G. Tumarkin, and R. J. Archuleta (1996). What is a reference site? *Bull. Seismol. Soc. Am.* **86,** no. 6, 1733–1748.

Street, R., Z. Wang, E. Woolery, J. Hunt, and J. Harris (1997). Site effects at a vertical accelerometer array near Paducah, Kentucky, *Eng. Geol.* **46,** 349–367.

Woolery, E. W., Z. Wang, N. S. Carpenter, R. Street, and C. Brengman (2016). The Central United States Seismic Observatory: Site characterization, instrumentation, and recordings, *Seismol. Res. Lett.* **87,** 215–228.

Zandieh, A., and S. Pezeshk (2011). A study of horizontal-to-vertical component spectral ratio in the New Madrid seismic zone, *Bull. Seismol. Soc. Am.* **101,** no. 1, 287–296.

Kentucky Geological Survey
University of Kentucky
228 Mining and Mineral Resources Building
Lexington, Kentucky 40506-0107
seth.carpenter@uky.edu
zmwang@uky.edu
(N.S.C., Z.W.)

Department of Earth and Environmental Sciences
University of Kentucky
101 Slone Research Building
Lexington, Kentucky 40506-0053
woolery@uky.edu
(E.W.W.)

Institute of Crustal Dynamics
China Earthquake Administration
No. 1 Anningzhuang Road, Haidian District
Beijing 100085
People's Republic of China
waltrong@126.com
(M.R.)

Manuscript received 26 May 2017;
Published Online 27 March 2018